In-out charge exchange measurements and 3D modelling of diagnostic thermal neutrals to study edge poloidal impurity asymmetries

D.J. Cruz-Zabala[1,2], E. Viezzer[1,2], U. Plank[3], R. M. McDermott[3], M. Cavedon[4], E. Fable[3], R. Dux[3], P. Cano-Megias[5,2], T. Pütterich[3], A. Jansen van Vuuren[1,2], M. Garcia-Munoz[1,2], J. Garcia Lopez[1,2] and the ASDEX Upgrade Team[6]

[1]Department of Atomic, Molecular and Nuclear Physics, University of Seville, Seville, Spain
[2]CNA (U. Sevilla, CSIC, J. de Andalucia), Seville, Spain
[3]Max-Planck-Institut für Plasmaphysik, Garching, Germany
[4]Dipartimento di Fisica "G. Occhialini", Università di Milano-Bicocca, Milano, Italy
[5]Department of Energy Engineering, University of Seville, Seville, Spain
[6]See author list of H. Meyer et al. 2019 Nucl. Fusion 59 112014

E-mail: dcruz3@us.es

February, 2022

Abstract. A new method was developed to model the neutral population produced by the gas puff based Charge Exchange Recombination Spectroscopy (CXRS) systems at ASDEX Upgrade (AUG). With this method, the edge impurity density on the High Field Side (HFS) and Low Field Side (LFS) can be obtained without the need to apply a Neutral Beam Injection (NBI) system. The neutral penetration needed for the calculation of the impurity density is obtained with a new gas puff module implemented in the FIDASIM code. The LFS impurity density profile evaluated with the new gas puff module matches the impurity density calculated with standard beam-based charge exchange diagnostics. Impurity temperature, rotation and density profiles at the HFS and LFS of an AUG H-mode discharge are presented. Edge impurity toroidal and poloidal flows show asymmetric structures. The impurity density asymmetries obtained with the new gas puff module are consistent with the observed flow structure.

Keywords: impurity, asymmetry, CXRS

1. Introduction

Impurity studies are key for determining the plasma confinement and fusion performance. Impurities will play a crucial role in future fusion devices reducing the thermal loads to the first wall via radiation. Furthermore, they are an important ingredient to reach divertor detachment [1]. Hence, measurements of how the impurities distribute across the poloidal plane are desirable for the success of future fusion reactors. Plasma diagnostic capabilities need to evolve to meet these needs. The Charge eXchange Recombination Spectroscopy (CXRS) [2] technique is well established in most of today's fusion devices for obtaining the impurity temperature, rotation and density. This technique exploits the light emitted after an electron transfer from an injected neutral particle (D) into an excited state of an impurity ion (A) of the plasma with charge state Z:

$$A^{Z+} + D \rightarrow A^{(Z-1)+*} + D^{+} \rightarrow A^{(Z-1)+} + D^{+} + h\nu$$

The measured spectral line gives information on the original impurity (A^{Z+}) temperature, rotation and density. Most of the CXRS systems exploit the neutrals injected by a Neutral Beam Injection system (NBI). However, not all fusion devices have NBI systems and those that do, do not necessarily use them in all their scenarios. A technique that complements NBI-CXRS (or beam based CXRS) is gas puff based CXRS [3, 4]. These systems inject thermal neutrals to produce charge exchange reactions. Due to the low energy of the neutrals, the penetration is reduced and the measurements are only possible at the edge of the plasma. Furthermore, the neutrals are normally injected as molecules (usually D_2). These molecules produce a large number of emission lines that might need to be taken into account for determining the impurity profiles.

While the impurity temperature and rotation can be extracted directly from the CX line, the impurity density requires information on the distribution of the injected neutrals. Two approaches, as described in [5], can be used to get the neutral penetration into the plasma:

(i) The neutral penetration is modelled.

(ii) Spectroscopy measurements on a Balmer line are used to get the neutral emissivity profile.

The first approach requires a realistic model of the neutral source while the second one requires additional measurements on a second spectral line. The CHICA code [6] enables impurity density calculations using several methods to model the NBI neutrals. However, gas puff neutrals require a different treatment due to the differences in energy and in the geometry of the source [4].

In this work, a new gas puff module was implemented in the FIDASIM [7, 8] code in order to model the neutral population generated by the gas puff. Combined with the radiance of the investigated CX line, the impurity density can be determined.

Previous studies [5, 9] demonstrated the existence of asymmetries in the impurity flows and density between LFS and HFS. These studies can now be improved due to

the recent upgrade of the HFS gas puff based CXRS system [4] and a second new gas puff based CXRS system on the LFS [10]. The new HFS gas puff based CXRS system is composed by a new gas valve, a poloidal optical head and a toroidal optical head. The new gas valve provides a calibrated gas source with fast gas modulation (of the order of ms). Each optical head is composed by 16 lines of sight (LOS). The spatial resolution is 7 mm for the toroidal optical head and 5-19 mm for the poloidal optical head, depending on the LOS. The poloidal optical head covers around 7 cm of the plasma edge, while the toroidal optical head covers around 11 cm. The lowest exposure time achievable is 2.5 ms, but an exposure time of 4.0 ms is normally used to have a good signal-to-noise ratio. The minimum velocity that the system can distinguish is around 1 km/s while the minimum temperature is 50 eV. The new gas puff module enables impurity density measurements and will be used to study poloidal asymmetries between the HFS and LFS taking advantage of the two gas puff systems. Furthermore, a new multi Gaussian fit procedure has been developed to study the impact of molecular lines on the investigated active CX line.

This paper is organized as follows: section 2 describes the methodology followed in this paper. That section includes the interpretation of the gas puff based impurity spectrum, the description of the new gas puff module implemented in the FIDASIM code and the calculation of the impurity density using the CHICA code. In section 3, the asymmetries between the experimental HFS and LFS impurity profiles are discussed taking advantage of the CXRS measurements taken at the LFS and HFS during an AUG H-mode discharge. Strong asymmetries are found in the poloidal and toroidal rotations and in the impurity density profile. A summary and an outlook are given in section 4.

2. Methodology

2.1. Analysis of gas puff based CXRS spectra

Compared to beam based CXRS, gas puff based CXRS has some advantages and disadvantages. While beam based CXRS has to deal with charge exchange reactions of impurities with beam neutrals at three different energies, gas puff based CXRS only has to deal with one energy component. However, the injected neutrals, in our case D_2, are molecules and they produce a large number of emission lines that can contaminate the measured impurity line. Thus, the effect of the molecular lines needs to be assessed for the interpretation of the measured spectra. Additionally, the background emission needs to be subtracted . This is obtained by the fast modulation (of the order of ms) of the gas puff based CXRS systems at AUG.

Figures 1(a) and 1(b) show a comparison between the HFS spectra obtained in the confined region and in the scrape-off-layer (SOL) for the active CX lines of fully ionized nitrogen (NVII at 566.937 nm) and figures 1(c) and 1(d) for fully ionized boron (BV at 494.467 nm) lines. As the spectra shown in figure 1 were taken at the HFS, a decrease in the R coordinate means a displacement towards the SOL. The spectra in the SOL region,

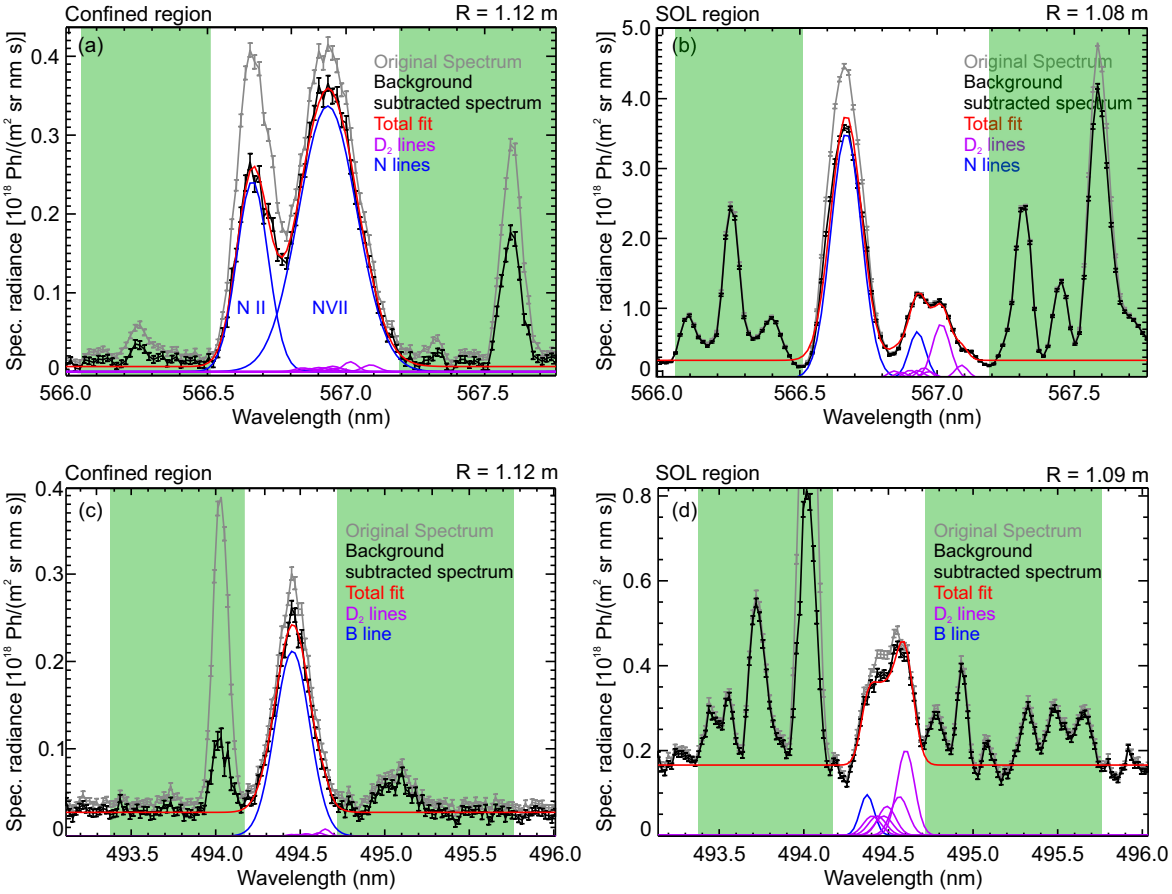

Figure 1. Figures a) and b) show the spectrum of the NVII line. Figures c) and d) show the spectrum of the BV line. Spectra of figures a) and c) are taken in the confined region and the spectra of figures b) and d) are taken in the near SOL. The molecular contribution is clear in figures b) and d). Green shaded areas have been ignored during the fit.

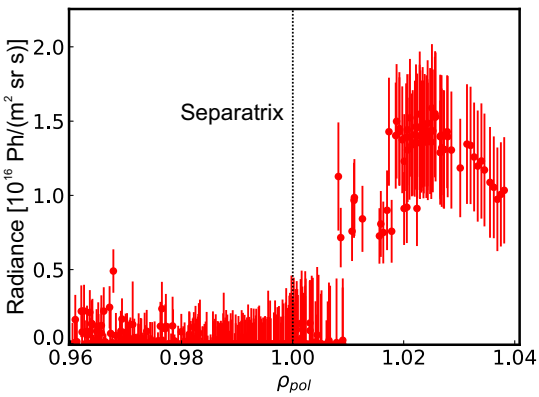

Figure 2. Measured radiance of the D_2 line at 567.1113 nm during a D_2 puff in an ELMy H-mode at AUG.

shown in figures 1(b) and 1(d), are clearly contaminated by molecular lines. Notice the change in the absolute emission when comparing the SOL and confined regions, specially for the nitrogen case. To account for the molecular lines, a multi Gaussian fit has been developed. The molecular database in [11] has been used to get the position of the deuterium molecular lines in the wavelength range of the analysed impurity spectral line. In the fitting routine it is imposed that all the molecular lines must have the same velocity and temperature and a fixed intensity relation. The temperature of these molecular lines is constrained to be lower than 3 eV, which is very low compared to the impurity temperatures (which is of the order of a few hundreds of eV). A shift of around 0.02 nm in the wavelength of the molecular lines is needed to describe the spectrum in the nitrogen case. This shift is the same for all the molecular lines and it might come from uncertainties in the rest wavelengths on the molecular database [11]. In the boron case, the molecular lines do not need any additional shift to describe the spectrum. The results of the multi Gaussian fit are also shown in figure 1. The new multi Gaussian fit procedure is able to describe the molecular contribution to the experimental spectra. However, due to the low dissociation energy of the molecules (≈ 3 eV), it is expected that only the LOS that are viewing the SOL or very close to the separatrix are affected by molecules. It should be noted that, even if all LOS explore a certain region of the SOL, not all of them go through the gas puff in the SOL. It is very important to describe the molecular contribution well in order to know in which radial range the molecules play a role. Figure 2 shows the radiance profile of the D_2 line at 567.1113 nm during a D_2 puff plotted against the normalized poloidal flux coordinate ρ_{pol}. At around $\rho_{pol} = 1.01$, i.e. in the near SOL, the radiance drops by one order of magnitude compared to the SOL further outside. This indicates that the molecules do not play an important role further inside the plasma. As the molecular contribution plays a minor role in the confined region, the spectra in this region can be fitted without considering the molecular lines. Note that this applies to the H-mode plasmas analysed here. In the next section, the new 3D model developed to simulate gas puff neutrals is presented.

2.2. Gas puff modelling using FIDASIM

The impurity density can be calculated from the radiance of the CX emission lines and the density of the injected neutrals. In this work, the FIDASIM code [7, 8] has been extended to include a gas puff module that models thermal neutrals with the geometry of the gas cloud. In its original version, the FIDASIM code models the neutral populations produced by the NBI in order to calculate the Fast-Ion D-alpha (FIDA) emission. The code is based on the tracking of Monte Carlo markers in a 3D grid. Initially, the markers are generated following a realistic description of the NBI system. Then, the markers are followed and a collisional radiative model is applied to calculate the neutral density and the FIDA emission produced by the NBI system. During this work, a new module has been implemented to initialize the Monte Carlo markers modelling the gas cloud shape that was determined in laboratory tests before the installation of the gas valve

in the vessel of AUG. In these tests, a camera recorded the gas injection during a glow discharge in a vacuum chamber. This enabled the calculation of the opening angle of the gas cloud for different gas species (D_2, He, N_2 and Ar). Furthermore, thanks to the temperature and pressure sensors of the vacuum chamber, a relation between the pressure inside the gas system and the gas flow rate injected by the valve was obtained [4]. Both the opening angle of the gas cloud and the gas flow rate are inputs of the new module implemented in the FIDASIM code.

The new gas puff module launches Monte Carlo markers with a certain angle with respect to the injection direction that is generated using a normal distribution. The standard deviation σ of the normal distribution is chosen such that it matches the opening angle θ_{lab} measured during the laboratory test of the gas puff valve:

$$\sigma = \frac{\theta_{lab}}{\sqrt{2 \cdot ln(2)}} \tag{1}$$

where θ_{lab} is 25° for D_2. The 3D initial unit vector velocity distribution for 500 markers is shown in figure 3. The z axis goes in the injection direction. The shape of the gas cloud, measured during the laboratory test, is also plotted in the background. As commented above, another needed input is the flow rate of the gas valve. In this work, it is assumed that each D_2 molecule dissociates isotropically into two atoms before reaching the separatrix [3]. Figure 2 shows that most of the molecules dissociate before reaching the separatrix. In order to simplify the module, it is assumed that each injected molecule produces an atom towards the plasma. This reasoning implies that the molecular flow rate measured in the laboratory will be equal to the atomic flow rate used in FIDASIM. The magnitude of the initial velocity of the Monte Carlo markers is also needed for the simulations. This is the only free parameter in the new module. The assumption of adiabatic expansion establishes an upper limit for the injection velocity of around 2000 m/s. Including effects like friction would reduce this value. The simulations show that an injection velocity of 2000 m/s produces impurity density profiles that are underestimated by around 50 %. Because of this, the velocity was adjusted to match the well established beam based impurity density calculation. The value of 100 m/s was found to be the most suitable one. This value might be lower than the real injection velocity, but it might compensate the possibility that not all the injected molecules produce a neutral atom going towards the plasma. Even if the velocity was reduced by a factor of 20 compared to the upper limit established by theory, this was translated in a change of around 50 % in the impurity density profile, demonstrating that this parameter does not have a strong impact in the thermal neutral modelling. The shape of the impurity density profile did not change much with velocities in the range of 100-2000 m/s. The changes in the velocity were translated into different absolute values of the impurity density profile.

Apart from the scan in the injection velocity value, several convergence tests have been performed varying the grid resolution, the number of markers, the opening angle and the gas flow rate. The grid was chosen such that it covers the intersection of the LOS with the gas cloud. The optimum value of the volume of each grid cell was found to

be 30 mm^3. This value was obtained as a compromise between computational time and convergence of the results. The number of markers used in the new gas puff module is 10^5. The opening angle of the gas cloud does not show a strong impact on the impurity density calculation, in agreement with [3, 5]. Scans in the gas flow rate show a linear dependence of the neutral density with the input flow rate.

Once the markers are initialized, the collisional radiative model of FIDASIM is applied to obtain the density of the first generation of neutrals. Additional neutrals are generated due to CX of main ions with the injected neutrals. These neutrals are called halo neutrals because they produce a cloud of thermal neutrals around the first generation of neutrals. Halo neutrals have to be treated in different steps, as additional generations of halo neutrals can be produced. These CX processes between main ions and halo neutrals will not increase the number of neutrals, but the energy distribution of the neutrals can change [7]. Figure 4(a) shows an example of the gas puff neutrals (first generation of neutrals) and (b) the halo neutrals generated by the HFS gas puff for a typical ELMy H-mode at AUG (#37529). The grey lines represent ρ_{pol}= 1.00, 0.99, 0.98 and 0.97. The poloidal LOS are plotted in yellow and the intersections of the toroidal LOS with the toroidal plane at the gas puff position are plotted with green crosses. Note that the poloidal LOS in reality end up in the upper divertor but they are plotted up to their associated measurement position for clarity. In agreement with [12], most of the injected neutrals are ionized before penetrating the separatrix. The halo neutrals are the population penetrating the plasma, i.e. they produce most of the CXRS signal. In the next section, the calculation of the impurity density profile using the neutral population modelled with FIDASIM is presented.

2.3. Impurity density calculation using gas puff modelling

The new gas puff module of FIDASIM introduced above, together with the geometry of the HFS and LFS gas puff based CXRS diagnostics, has been implemented in the CHICA code [6] environment. With the new gas puff module in FIDASIM, CHICA is now able to calculate the impurity density from beam-based CXRS and gas puff-based CXRS. The CHICA code considers the geometry of the CXRS diagnostics to compute the integral of the neutral density (given by FIDASIM) along the LOS. Furthermore, CHICA reads the spectral radiance from the CXRS diagnostic and it calculates the impurity density following:

$$n_\alpha = \frac{4\pi}{h\nu} \frac{L_{CX,\alpha,\lambda}}{\sum_n \int_{LOS} n_{D,n}(s) \langle \sigma_{n,\alpha,\lambda} v_j \rangle_{eff}(s) ds} \tag{2}$$

where $h\nu$ is the energy of the photons, $L_{CX,\alpha,\lambda}$ is the experimentally determined radiance of the investigated spectral line, $n_{D,n}(s)$ is the neutral density at each point s along the LOS, $\langle \sigma_{n,\alpha,\lambda} v_j \rangle_{eff}$ is the effective CX emission rate with $\sigma_{n,\alpha,\lambda}$ the cross section and v_j the collision velocity. Here, the subindex n is the principal quantum number. For gas puff based CXRS, the neutral population with n=2 is dominant in the CX process [3]

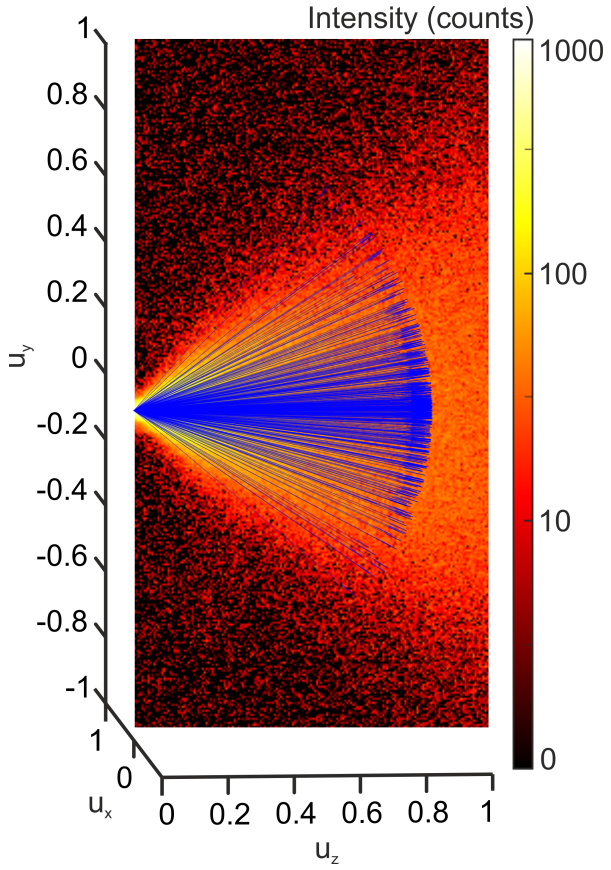

Figure 3. Blue arrows represent the initial distribution of unit vectors of 500 markers produced by the new gas puff module of FIDASIM. The background picture represents the gas cloud produced by the HFS gas puff observed during a laboratory test before its installation in AUG. This picture was taken recording the emission of the gas puff during a glow discharge in a vacuum chamber.

and thus, needs to be included in the calculation of the impurity density. This equation considers that the impurity density is constant along the LOS. The cross-sections are taken from the cross-section data implemented in the CHICA code which are mostly based on the ADAS database [13]. The angle brackets $\langle ... \rangle$ in equation (2) represent the integration over the velocity distributions: thermal velocity distribution in the case of halo and relative reaction velocity in the case of beam (gas puff in this case) impact charge exchange. In the gas puff case, the thermal velocity of the impurities is much bigger than the velocity of the injected neutrals. Thus, the relative reaction velocity is given by the impurity temperature. Figure 5 shows a comparison of the reconstructed LFS edge impurity density profiles from beam and gas puff based CXRS in two H-mode discharges: in #37529, nitrogen was the investigated impurity, and in #38002, it was boron. Good agreement of the impurity density profile, obtained with gas puff-based CXRS and with standard beam-based CXRS, is observed. This validates the new gas puff module implemented in the FIDASIM code and the coupling of this module with the CHICA code. This new module expands the experimental capabilities, since it

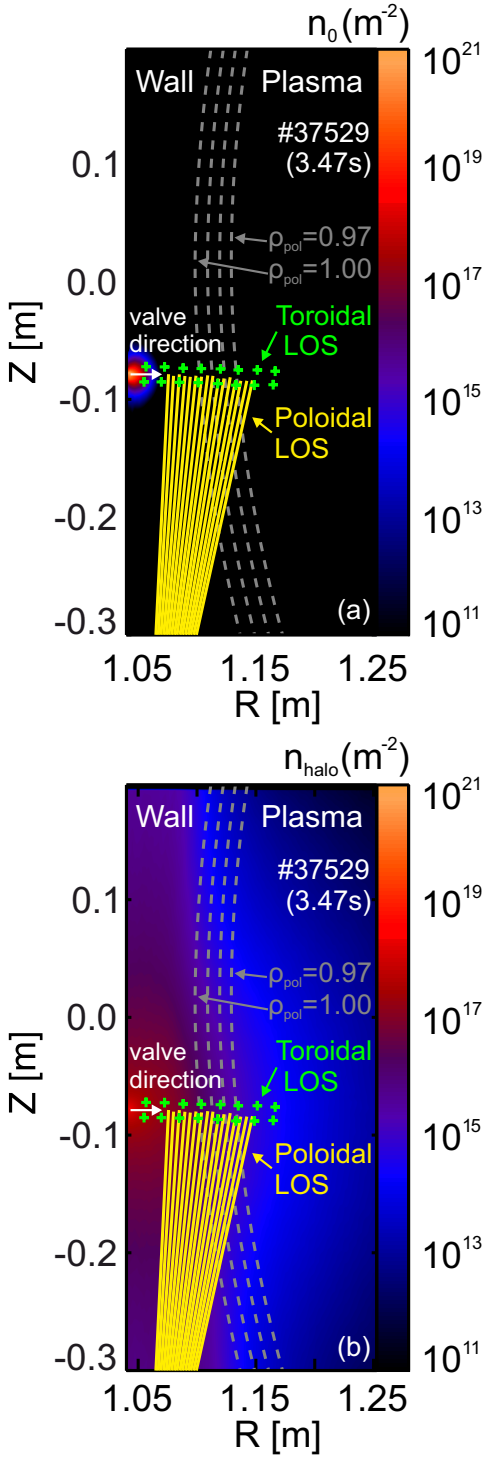

Figure 4. First generation of gas puff neutrals (a) and halo neutrals (b) obtained with the new gas puff module implemented in FIDASIM for AUG discharge #37529.

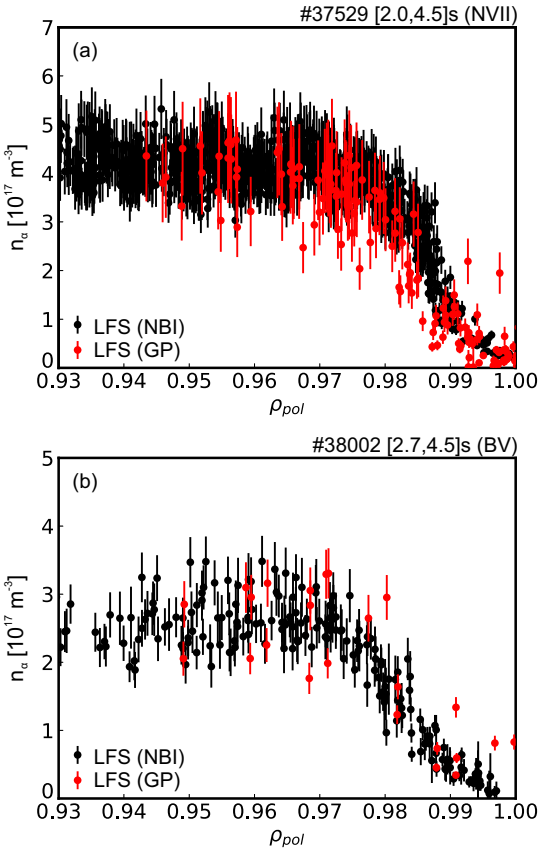

Figure 5. Impurity density profile obtained with beam based CXRS (black) and gas puff based CXRS (red) for AUG discharges #37529 (a) and #38002 (b). (a) shows the nitrogen density profile, while (b) shows the boron density profile.

allows for the calculation of the edge impurity density profile without the need of NBI application.

3. Experimental results

3.1. Profile comparison between HFS and LFS

Figure 6 shows the inter-ELM nitrogen temperature, toroidal rotation and poloidal rotation profiles measured on the NVII line (566.937 nm) in an H-mode discharge (#37529) at AUG. In this discharge, the plasma current was 1.0 MA and the toroidal magnetic field on-axis was -2.5 T. 4.85 MW of NBI and 1.35 MW of Electron Cyclotron Resonance Heating (ECRH) were applied. The central electron density was about $9{\cdot}10^{19}$ m^{-3} while the electron density at the pedestal top was around $6.5{\cdot}10^{19}$ m^{-3}.

Radial shifts of a few millimetres are normally required to align the profiles due to uncertainties in the equilibrium reconstruction and in the LOS geometry calibration. The first step for the alignment is to shift the electron profiles such that the electron temperature is $\sim$ 100 eV at the separatrix position [14, 15]. Then, the LFS CXRS diagnostics are shifted such that the maximum impurity temperature gradient matches

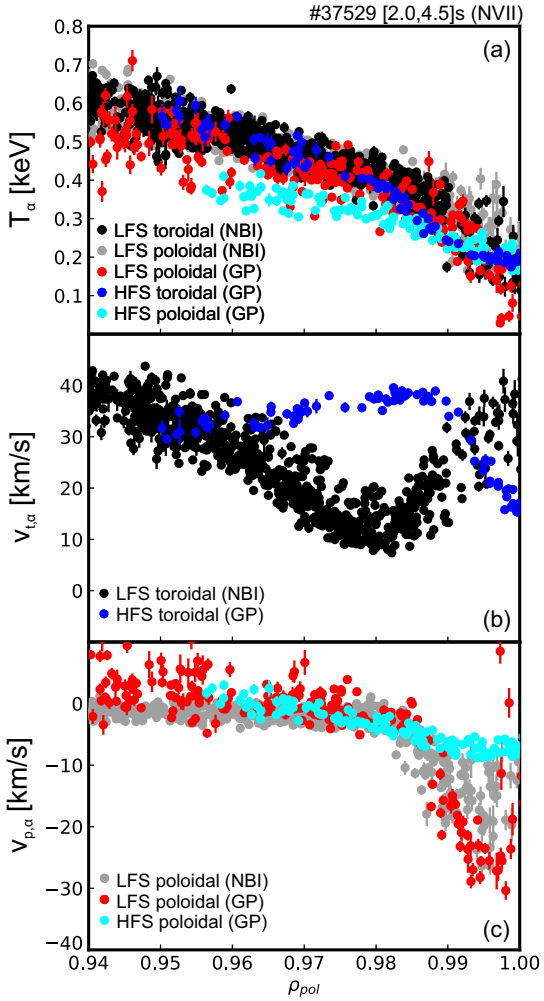

Figure 6. H-mode temperature (a), toroidal rotation (b) and poloidal rotation (c) profiles of N at the LFS and HFS in AUG discharge #37529.

the maximum electron temperature gradient [16]. Then, the HFS and LFS diagnostics are aligned matching the position of the minimum in the poloidal rotation. In section 3.2, it will be shown that, doing this alignment, $E_r/(RB_p) = -\partial\phi/\partial\psi$ is a flux function. A shift of 2 mm has been applied to the HFS toroidal and poloidal CXRS diagnostics, while a shift of -1 mm and +2 mm have been applied to the LFS toroidal and LFS poloidal CXRS diagnostics, respectively. The impurity temperature pedestal top seems to be in a slightly different position at the HFS and LFS (see figure 6(a)). However, both profiles match within the data scattering. At Alcator C-Mod, this effect was found to be much stronger [17]. The separatrix temperature is better resolved at the HFS. The spatial resolution of the HFS poloidal diagnostic worsens towards the inner region of the plasma producing a deviation in the measured temperature at $\rho_{pol} < 0.98$ compared to the rest of the diagnostics. The toroidal velocities show an asymmetry when comparing LFS and HFS, as observed before [5, 9, 18]. While the LFS toroidal velocity has a clear minimum at around 0.98, the HFS toroidal velocity has a maximum at around 0.99. Both poloidal velocity profiles have a negative minimum with different values. In this

work, negative poloidal velocities go in the electron diamagnetic drift direction. The LFS poloidal velocity reaches a minimum of about -20 to -30 km/s and the HFS poloidal velocity has a minimum of about -9 km/s. These flow asymmetries are in agreement with previous studies [5, 9, 18].

3.2. Poloidal impurity density asymmetries

In this section, the asymmetries in the impurity density profile are discussed. Density and flow profiles are related by the continuity equation, which establishes that the divergence of the particle flux should be zero in the absence of neutral sources ($\nabla\cdot(n\mathbf{v}) = 0$). The general expression for a divergence free flow neglecting neutral sources and radial flows can be written as [9, 19, 20]:

$$\mathbf{v}_\alpha = \omega_\alpha R\mathbf{e}_t + \frac{K(\psi)}{n_\alpha}B\mathbf{e}_\parallel \tag{3}$$

where $K(\psi)$ is a flux function, R is the major radius, B is the magnetic field, $\mathbf{e}_t$ is the unit vector along the toroidal direction, $\mathbf{e}_\parallel$ is the unit vector in the parallel direction to the magnetic field and $\omega_\alpha = -\frac{\partial\phi}{\partial\psi} - \frac{1}{eZ_\alpha n_\alpha}\frac{\partial p_\alpha}{\partial\psi}$. Note that the poloidal component of the velocity is included in the parallel term as $\mathbf{e}_\parallel = \frac{B_t}{B}\mathbf{e}_t + \frac{B_p}{B}\mathbf{e}_p$ with $\mathbf{e}_p$ being the unit vector in the poloidal direction and B_t and B_p the toroidal and poloidal magnetic fields, respectively. The first term of ω_α corresponds $E_r/(RB_p) = -\partial\phi/\partial\psi$, which to lowest order is a flux function as the electrostatic potential is also a flux function [19]. The radial electric field is given by the radial force balance equation:

$$E_r = \frac{\nabla p_\alpha}{eZ_\alpha n_\alpha} - v_{p,\alpha}B_t + v_{t,\alpha}B_p \tag{4}$$

where p_α, n_α, $v_{t,\alpha}$ and $v_{p,\alpha}$ are the pressure, density, toroidal rotation and poloidal rotation of the species α, respectively. Figure 7 shows that $E_r/(RB_p)$ is a flux function within the uncertainties if we use the profiles shown in figures 5(a) and 6. In the presence of impurity density asymmetries, $\omega_\alpha = \frac{E_r}{RB_p} - \frac{1}{eZ_\alpha n_\alpha}\frac{\partial p_\alpha}{\partial\psi}$ is not a flux function as n_α appears in the pressure gradient term. Taking the toroidal component of equation (3), we get:

$$\frac{n_\alpha}{K(\psi)} = \frac{1}{(v_{t,\alpha} - \omega_\alpha R)\frac{1}{B_t}} \tag{5}$$

If we take the previous equation at the LFS and HFS, an expression for the ratio between the impurity density at HFS and LFS can be obtained:

$$\frac{n_\alpha^{HFS}}{n_\alpha^{LFS}} = \frac{((v_{t,\alpha} - \omega_\alpha R)\frac{1}{B_t})^{LFS}}{((v_{t,\alpha} - \omega_\alpha R)\frac{1}{B_t})^{HFS}} = \frac{v_{p,\alpha}^{LFS}B_p^{HFS}}{v_{p,\alpha}^{HFS}B_p^{LFS}} \tag{6}$$

This equation provides the ratio between impurity densities as a function of poloidal flows and magnetic fields if neutral sources and radial flows are neglected. From this equation, the expected poloidal velocity without impurity density asymmetries can be estimated. Figure 8 shows the measured and expected HFS poloidal velocities, assuming that the impurity density profile is symmetric ($v_{p,no\,asy}^{HFS} = v_p^{LFS}\frac{B_p^{HFS}}{B_p^{LFS}}$). Both curves are

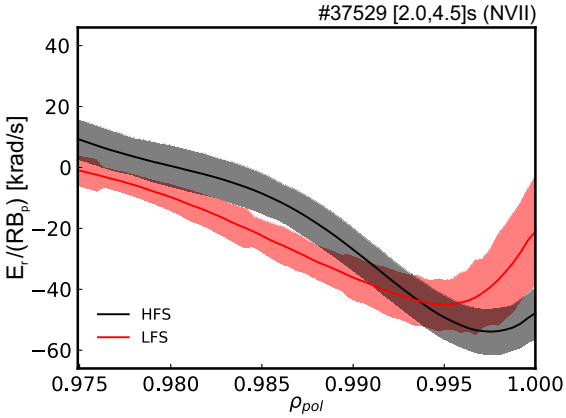

Figure 7. E_r/RB_p at the HFS and LFS. It is observed that this quantity is a flux function within the uncertainties.

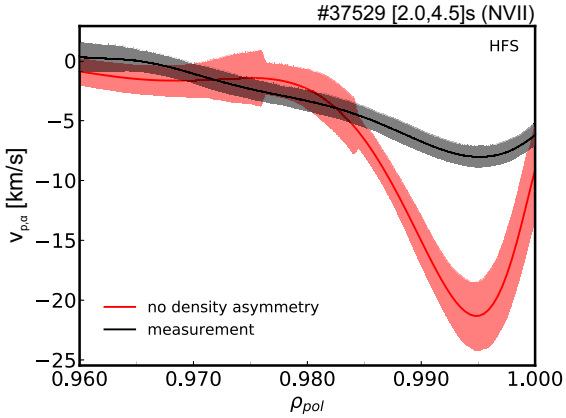

Figure 8. Experimental and expected assuming constant impurity density along the flux surface HFS poloidal velocities.

different in the region of the minimum, suggesting that an impurity density asymmetry exists there. The flux function $E_r/(RB_p)$ also allows us to relate HFS and LFS densities:

$$\begin{aligned}
&\left(\frac{E_r}{RB_p}\right)^{LFS} = \\
&= \left(\frac{\nabla p_\alpha}{eZ_\alpha n_\alpha RB_p} - \frac{v_{p,\alpha}B_t}{RB_p} + \frac{v_{t,\alpha}}{R}\right)^{LFS} = \\
&= \left(\frac{\nabla p_\alpha}{eZ_\alpha n_\alpha RB_p} - \frac{v_{p,\alpha}B_t}{RB_p} + \frac{v_{t,\alpha}}{R}\right)^{HFS} = \\
&= \left(\frac{E_r}{RB_p}\right)^{HFS}
\end{aligned} \tag{7}$$

This equation has to be integrated to determine the impurity density at the HFS. Specifically, the following equation has to be solved to obtain the impurity density at the HFS:

$$\frac{1}{n_\alpha^{HFS}}\frac{\partial n_\alpha^{HFS}}{\partial r^{HFS}} =$$

$$= \left\{ \left[\left(\frac{E_r}{RB_p} \right)^{LFS} - \omega_\alpha^{HFS} \right] eZ_\alpha R^{HFS} B_p^{HFS} - \nabla T_\alpha^{HFS} \right\} \frac{1}{T_\alpha^{HFS}} =$$
$$= D(r^{HFS}) \tag{8}$$

The solution of this equation is:

$$n_\alpha^{HFS}(r^{HFS}(\rho)) = n_\alpha^{HFS}(r_0^{HFS}(\rho_0)) \cdot exp \left[\int_{r'=r_0^{HFS}(\rho_0)}^{r'=r^{HFS}(\rho)} D(r')dr' \right] \tag{9}$$

The difference between this equation and equation (6) is that this equation is exact, while equation (6) is neglecting effects due to sources and radial terms. However, even if this equation is exact, it is not very suitable to compute the asymmetries because the exponential is prone to large uncertainties due to the propagation of the uncertainties inside the gradients and the resulting expression. Furthermore, this equation needs a boundary condition, $n_\alpha^{HFS}(r_0^{HFS}(\rho_0))$, due to the integration.

Figure 9(a) shows a comparison between the impurity density at the HFS and at the LFS, both obtained from gas puff based CXRS diagnostics [4, 10] using the new gas puff module implemented in FIDASIM. At the pedestal top, both profiles still match, while towards the separatrix, the HFS impurity density is higher than the LFS one. In figure 9(b), the asymmetry factor $n_\alpha^{HFS}/n_\alpha^{LFS}$ obtained from the HFS and LFS impurity densities is shown, together with the asymmetry factor based on the poloidal impurity flow measurements using equation (6). Both curves match within the uncertainties and show an accumulation of impurities at the HFS. It is also shown in red, the asymmetry factor obtained using equation (9) taking into account the uncertainties in the flux function $E_r/(RB_p)$. Good agreement with the asymmetry factors from densities and poloidal flows is found. The experimental impurity density at the HFS at $\rho_{pol} = 0.98$ was used as the boundary condition in this case. This curve stops at $\rho_{pol} = 0.995$ due to the large uncertainties caused by the error propagation inside the gradients in the region $0.995 \leq \rho_{pol} \leq 1.0$. The accumulation of impurities at the HFS edge is consistent with previous studies [5, 9]. Compared to previous work [21], the agreement between the asymmetries obtained with the flows and with the densities is improved. As mentioned in section 3.1, the higher impurity density at the HFS compared to the LFS is the reason why the separatrix temperature is better determined at the HFS compared to the LFS. Further impurity asymmetry studies in different scenarios including plasmas without NBI are the subject of future work.

4. Summary and Outlook

A new module simulating the injection of gas puff neutrals has been included in the FIDASIM code in order to shed light on the edge poloidal impurity density asymmetries. This module simulates the penetration of thermal neutrals and provides the first neutral generation and the subsequent halo neutral distributions. A new approach to study the impact of molecular lines has been followed in this work: molecular lines in the vicinity of the impurity spectral line are fitted, with constraints in the shifts, heights

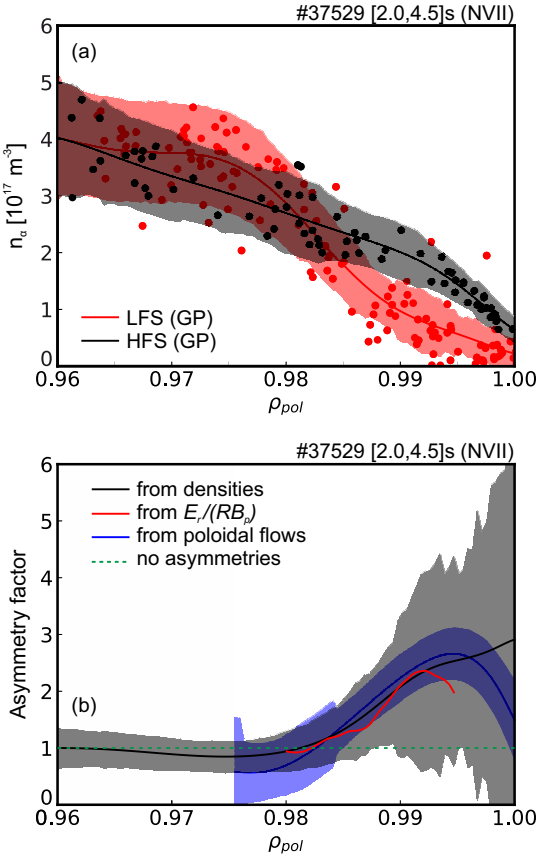

Figure 9. Figure (a) shows the impurity density profiles at the LFS (red) and HFS (black). Figure (b) shows the asymmetry factor obtained from the flows, from the densities and from equation (7).

and widths of their Gaussian fits. In H-mode plasmas, the molecular emission from the gas puff itself only affects the SOL region. In the confined region, the velocity profiles show asymmetries that can be explained in terms of the existence of an impurity density asymmetry [5, 9, 18]. The asymmetry factor $n_\alpha^{HFS}/n_\alpha^{LFS}$ is estimated in three different ways: from the impurity flow measurements, from $E_r/(RB_p)$ and from the measured impurity densities (employing the new gas puff module). All three methods show good agreement within the experimental uncertainties. For the calculation of the impurity density, the emissivity of the impurity spectral line is taken from the CXRS measurements. The impurity density obtained with the new gas puff module has been compared with the profiles obtained with well established beam-based CXRS systems at the LFS and show excellent agreement. This validates the new module, which allows us to extend impurity density studies to plasma scenarios without the need to apply a neutral beam. Furthermore, this new approach opens the possibility to obtain edge impurity density measurements in regions of the plasma which are not suitable for the installation of an NBI system.

Acknowledgments

This work received funding from the VI Plan Propio de Investigación de la Universidad de Sevilla (PPITUS 2017).

The support from the European Research Council (ERC) under the European Union's Horizon 2020 research and innovation programme (grant agreement No. 805162) is gratefully acknowledged.

This work has been carried out within the framework of the EUROfusion Consortium and has received funding from the Euratom research and training programme 2014–2018 and 2019–2020 under grant agreement No. 633053. The views and opinions expressed herein do not necessarily reflect those of the European Commission.

References

[1] A. Kallenbach *et al.* *Nuclear Fusion*, 55:053026, 2015.
[2] R.J. Fonck, D.S Darrow, and K.P Jaehnig. *Phys. Rev. A*, 29:3288, 1984.
[3] R.M. Churchill *et al.* *Rev. Sci. Instrum.*, 84:093505, 2013.
[4] D.J. Cruz-Zabala *et al.* *Journal of Instrum.*, 14:C11006, 2019.
[5] E. Viezzer *et al.* *Plasma Phys. Control. Fusion*, 55:124037, 2013.
[6] R.M. McDermott *et al.* *Plasma Phys. Control. Fusion*, 60:095007, 2018.
[7] W.W. Heidbrink, D. Liu, E. Ruskov, and B. Geiger. *Commun. Comput. Phys.*, 10:716, 2011.
[8] B. Geiger *et al.* *Plasma Phys. Controlled Fusion*, 62:105008, 2020.
[9] T. Pütterich *et al.* *Nuclear Fusion*, 52:083013, 2012.
[10] U. Plank *et al.* *Rev. Sci. Instrum.*, In preparation.
[11] R.S. Freund, J.A. Schiavone, and H.M. Crosswhite. *J. Phys. Chem. Ref. Data*, 14:235, 1985.
[12] B. Lipschultz, D. Whyte, and B. LaBombard. *Plasma Phys. Controlled Fusion*, 47:1559, 2005.
[13] H.P. Summers. The adas user manual version 2.6. 2004.
[14] J. Neuhauser *et al.* *Plasma Phys. Controlled Fusion*, 44:869, 2002.
[15] A. Kallenbach *et al.* *Nuclear Fusion*, 43:573, 2003.
[16] E. Viezzer *et al.* *Nuclear Fusion*, 53:053005, 2013.
[17] R.M. Churchill *et al.* *Physics of Plasmas*, 22:056104, 2015.
[18] R.M. Churchill *et al.* *Nuclear Fusion*, 53:122002, 2013.
[19] F.L. Hinton and R.D. Hazeltine. *Rev. Mod. Phys.*, 48(2), 1976.
[20] K.D. Marr *et al.* *Plasma Phys. Control. Fusion*, 52:055010, 2010.
[21] E. Viezzer *et al.* *Nuclear Fusion*, 55:123002, 2015.